EDGE ARTICLE

Check for updates

The spin-coupling-dependent oxygen reduction mechanism in dual-atom catalysts

Mingyuan Yu, [abc] Erjun Kan [ID] *[abc] and Cheng Zhan [ID] *[abc]

The role of electronic spin in electrocatalysis has led to the emerging field of "spin-dependent electrocatalysis". While spin effects in individual active sites have been well understood, spin coupling among multiple sites remains underexplored in electrocatalysis, which will bring forth new active sites and mechanisms. In this work, we propose a general theory to understand the spin coupling in electrocatalysis. Inspired by spintronics, the energy of the spin-polarized bond of catalyst–adsorbate can be effectively tuned by exchange splitting, resulting in a spin-dependent mechanism. To validate this hypothesis, we take the Fe_2N_6 dual-atom-catalyst (DAC) with parallel and antiparallel spin (PS/APS) alignments as an example. Our calculation demonstrates that spin exchange splitting significantly determines the ORR mechanism, leading to a huge discrepancy in ORR activity in APS-Fe_2N_6 ($U_L = 1.04$ V *vs.* SHE) and PS-Fe_2N_6 ($U_L = 0.67$ V *vs.* SHE). We further reveal that PS alignment enhances exchange splitting and strengthens OH/O_2 adsorption, while APS alignment reduces exchange splitting and weakens OH/O_2 adsorption. This mechanism is further validated with other bi-metallic DACs. Our work first unravels how spin exchange splitting alters the catalytic activity and mechanism, offering significant mechanistic insights into spin-related electrocatalysis.

Introduction

Transition metal-based single-atom and dual-atom catalysts (SACs and DACs, respectively) have shown great potential in electrocatalysis due to their high activity, selectivity as well as highly tunable coordination environment.[1-10] In these catalysts, due to the magnetism of 3d/4d/5d transition metals, the spin state of the active center significantly influences the catalytic mechanism and activity. In recent years, spin-related effects have become a hot topic in both experimental and theoretical electrocatalysis, bringing forth a new subfield called "spin-dependent electrocatalysis".[11,12] For instance, recent experiments have revealed that the spin state manipulation of the Fe center by introducing Fe clusters greatly promotes the oxygen reduction reaction (ORR) activity of the Fe–N–C SAC.[13,14] A similar strategy in the Mn-based SAC for the ORR was reported by Liu *et al.*, which controls the spin state by S doping.[15] Tuning the spin by chemical modification has become a useful strategy to improve the activity or selectivity in electrocatalysis.[16-19] Although experimental studies have reported various ways to tune the spin state of SACs,[20-22] the correlation between the spin state and activity is not fully understood yet. To explore this

correlation, the first-principles density functional theory (DFT) combined with scaling relation analysis has been extensively used. A series of studies by Zhong *et al.* have reported that the magnetic moment on Fe exhibits a linear correlation to the O_2 adsorption energy in Fe–C_2N SACs.[23,24] Similar results were also found in FeN_4 and other TM-N-C SACs, which suggests the spin moment as a useful descriptor of ORR activity for individual active sites.[25,26] Moreover, an experimental study by Lu *et al.* found that the ferromagnetic–antiferromagnetic (FM–AFM) transition also significantly alters the activity of the oxygen evolution reaction (OER), which paves a new way to the spin manipulation in electrocatalysis.[27] The feasibility of this strategy has also been theoretically validated in ferromagnetic electrocatalysts.[28-30] To summarize, tuning the spin state of an individual active site or entire catalyst is an efficient strategy to optimize performance in electrocatalysis.

At the current stage, the spin effects on an individual active site (such as SACs) or FM/AFM-type catalysts have been well understood through electronic structure theory and descriptor analysis, while the spin coupling effect of multiple active sites has rarely been reported in electrocatalysis from either an experimental or theoretical perspective. Here, one should note that the spin coupling of multiple catalytic sites refers to the localized multiple spin states or spin alignments, which can be metastable and different from an individual site of SACs with spin multiplicity or an FM (or AFM) catalyst. An important concept of "inter-site distance effect" was proposed in highly dense Fe–N–C SACs by Jin *et al.*, who discovered that the Fe–Fe

School of Physics, Nanjing University of Science and Technology, Nanjing 210094, China. E-mail: czhan@njust.edu.cn; ekan@njust.edu.cn

bMIIT Key Laboratory of Semiconductor Microstructure and Quantum Sensing, Nanjing University of Science and Technology, Nanjing 210094, China

cEngineering Research Center of Semiconductor Device Optoelectronic Hybrid Integration in Jiangsu Province, Nanjing 210094, China

distance (from 50 Å to 5 Å) alters the magnetic moment and catalytic activity of Fe.[31] However, most studies on the spin effect usually default to a parallel spin arrangement of multiple sites and do not consider the effects of electrode potential and surface oxidation, leading to an incomplete mechanistic understanding of spin coupling effects in electrocatalysis. More importantly, a recent study has clearly revealed that the change of spin alignment by ferromagnetic–paramagnetic transition can significantly alter the reaction kinetics of ammonia synthesis on a Co catalyst, which underlines the crucial role of spin alignment in determining the catalytic activity.[32] Thus, from the theoretical side, a complete mechanistic understanding of spin coupling effects in electrocatalysis is extremely important to dissecting the spin-related catalytic mechanism and guiding the design of spin catalysts.

In this work, inspired by the fundamental spin coupling model in spintronics, we propose a general mechanism to understand the spin coupling effect of multiple active sites in electrocatalysis. For the intermediates with magnetism, the energy of spin-polarized bonding/antibonding orbitals of catalyst–adsorbate is proportionally determined by exchange splitting of neighboring sites, leading to the variation of activity. To validate this hypothesis, we use the graphene-based Fe_2N_6 DAC composed of two adjacent FeN_4 sites as an example and systematically study the effect of spin alignment on ORR mechanisms. Our simulation explicitly shows how the spin exchange splitting dominates the ORR mechanism by tuning the spin-polarized σ^*(Fe–O) bond. Our mechanistic understanding in this work not only reveals the spin coupling effects in the ORR mechanism of DAC but also potentially extends to the study of the catalytic activity of paramagnetic catalysts with tunable spin arrangements.

Methods

Spin-polarized DFT calculations were performed by using the Vienna *ab initio* simulation package (VASP).[33–35] In our DFT calculation, the exchange-correlation effect was treated by the general gradient approximation with the Perdew–Burke–Ernzerhof formalism (GGA-PBE).[36] The van der Waals interaction of adsorbates was described by the empirical correction in Grimme's scheme (DFT-D3).[37] The DFT + U method was employed to deal with the strong correlation effect in Fe with the $U_{eff} = U - J$ value set as 4.03 eV. According to our previous research and test calculation in Fig. S1, using HSE06 as the benchmark, this U_{eff} value can reliably predict the stability of different spin states while PBE cannot.[38] The electron–nucleus interaction was described by the Projector-Augmented Wave (PAW) pseudopotential.[33] The energy cutoff of the plane-wave basis set was set to 550 eV. The k-point sampling in the Brillouin zone was carried out using a gamma-centered $2 \times 2 \times 1$ mesh for geometry relaxation and a $10 \times 6 \times 1$ mesh for electronic structure calculation. The convergence criteria in our DFT calculation were 1×10^{-6} eV and 0.02 eV Å^{-1} for electronic and ionic optimization, respectively. The Fe–N–C DACs were modeled by an Fe_2N_6 site ($Fe_2N_6C_{10}$ model) embedded in monolayer graphene in an orthorhombic cell with the lattice

parameters $a = 9.84$ Å and $b = 17.04$ Å, as shown in Fig. 2a. A vacuum slab of 30 Å thickness in the z direction was introduced above the Fe_2N_6 model and filled with implicit electrolyte. The VASPKIT was used for electronic structure and density of states (DOS) analysis.[39] The LOBSTER package was used to analyze the Mulliken charge, bonding orbital and binding strength between Fe and adsorption *via* Crystal Orbital Hamiltonian Population (COHP) analysis.[40,41]

To calculate the adsorption free energy at a constant electrode potential, we adopted the method proposed by Duan and Xiao, in which the electron number and ionic coordinates were optimized simultaneously.[42] Implicit solvation based on a modified Poisson–Boltzmann equation was applied to describe the response behavior of electrolyte with respect to the applied potential.[43] The dielectric constant and Debye length of implicit electrolyte were set to 80 and 3 Å, respectively.[44] The calculated potential-dependent energies can be fit to a quadratic function with E as U:

$$E(U) = -\frac{1}{2}C(U - U_0)^2 + E_0 \tag{1}$$

where U_0 is the potential of zero charge (PZC), E_0 is the corresponding free energy in the neutral state, and C is the capacitance of the surface. The potential U was calculated under the reference of the standard hydrogen electrode (SHE). The fitted parameters for all the intermediates are listed in Tables S1 and S2. Based on eqn (1), the potential-dependent free energy was used to construct the free energy profile of the ORR and set up the micro-kinetics simulation under the reference of standard hydrogen electrode. All the detailed information is provided in the SI.

Results and discussion

A general mechanistic picture of spin coupling effects in electrocatalysis

In ferromagnetic (FM) and antiferromagnetic (AFM) materials, the density of states (DOS) usually shows a symmetric shape in the AFM state and an asymmetric shape in the FM state because of exchange splitting, as depicted in Fig. 1a (the alter magnetic case is not discussed in this work). The shifted peak in DOS is mainly attributed to the magnetic component of orbitals in the material, such as the d orbitals in 3d elements. Based on this point, the energy of the chemical bond with magnetism (partial filling of electrons as depicted by Fig. 1b) can be effectively altered by the spin exchange coupling from neighboring magnetic sites, which potentially leads to changes in catalytic activity and mechanism, as depicted in Fig. 1c. Taking the Fe–O bond as an example, our previous study on an FeN_4 SAC has clearly confirmed that the σ(Fe–OH) bond is indeed magnetic with the bond order of 0.5 in the ORR process.[45] Thus, it is expected that a strong exchange splitting (PS coupling) will elevate the energy of the unfilled spin-down σ^* orbital and lead to more difficult electron filling (right panel of Fig. 1c), while a weak exchange splitting (APS coupling) should weaken the Fe–O bond due to the easier electron filling in the σ^*(Fe–O) orbital (left panel of Fig. 1c). This spin-coupling-dominated energy shift of the σ^*
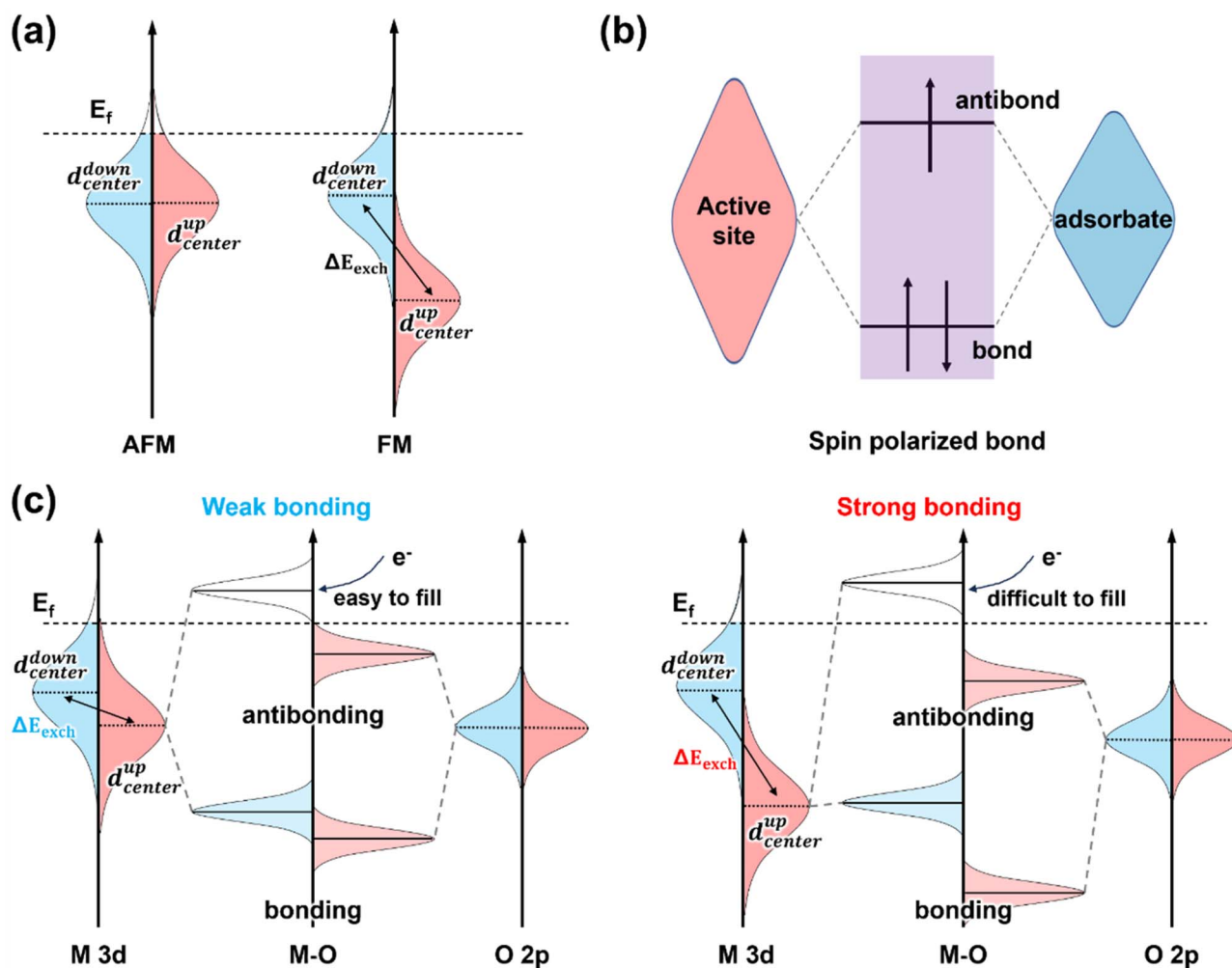
Fig. 1 Schematic description of: (a) ferromagnetic/antiferromagnetic materials; (b) spin-polarized bond of catalyst–adsorbate; (c) effect of spin exchange splitting on the M–O bond.

orbital will significantly influence the ORR activity and mechanism. To validate this hypothesis, we will use the graphene-based Fe_2N_6 DAC as a model system and comprehensively investigate how spin alignment determines the ORR mechanism in the next section.

Spin multiplicity and stability of APS/PS-Fe_2N_6

First, we performed structure relaxation on the Fe_2N_6C DAC consisting of two FeN_4 units connected *via* two N atoms, as shown in Fig. 2a. Each Fe in Fe_2N_6 has similar bonding and spin states to the FeN_4 SAC: the Fe is in dsp^2 hybridization and forms four σ(Fe–N) bonds with the sp^2 orbital of N, as shown in Fig. 2b.[45] Thus, there are three available spin states of Fe marked as $S = 2$ (high spin, HS), $S = 1$ (intermediate spin, IS) and $S = 0$ (low spin, LS), as shown in Fig. S2. Inspired by FM and AFM materials, various spin coupling modes should also exist in the Fe–N–C-type DACs, leading to various metastable PS- and APS-type Fe_2N_6 moieties. Through the occupation-controlled DFT calculation,[46,47] as listed in Table S3, we obtained nine spin states of APS/PS/non-magnetic Fe_2N_6 with their electronic

structure shown in Fig. 2c, d and S3–S5. (Partial occupation is marked by smaller arrows, which is unavoidable in periodic DFT calculation.) Comparing their neutral state energy in Table S3, it shows that Fe with LS or HS ($S = 0$ or 2) has much higher energy than IS ($S = 1$), which exhibits a similar feature to the FeN_4 SAC in our previous work.[45] Since a recent study has reported the IS–HS transition of FeN_4 at high potentials,[48] we additionally performed constant potential calculations on HS-Fe_2N_6, as shown in Fig. 2e and f. It shows that the HS-Fe_2N_6 (marked by APS-4 and PS-4, Fe is in $S = 2$ or $S = -2$) are not the most stable spin states in the ORR potential range. Thus, the possible existence of HS Fe in Fe_2N_6 DACs can be excluded. Finally, six spin states with IS state Fe were selected for further study: three APS cases (APS-1,2,3) and three PS cases (PS-1,2,3), as shown in Fig. 2c–f.

The electronic occupation of APS-/PS-Fe_2N_6 DACs (Fig. 2c and d) was obtained based on their PDOS in Fig. S3. As shown in Fig. 2c and d, the occupation of d orbitals in APS-1 and PS-1 can be assigned as $(d_{x^2-y^2})^2 (d_{xz})^2 (d_{z^2})^1 (d_{yz})^1 (d_{xy})^0$, while APS-2 and PS-2 show $(d_{x^2-y^2})^2 (d_{xz})^1 (d_{z^2})^2 (d_{yz})^1 (d_{xy})^0$ occupation on Fe. (Partial occupation is ignored here for convenience.) Different
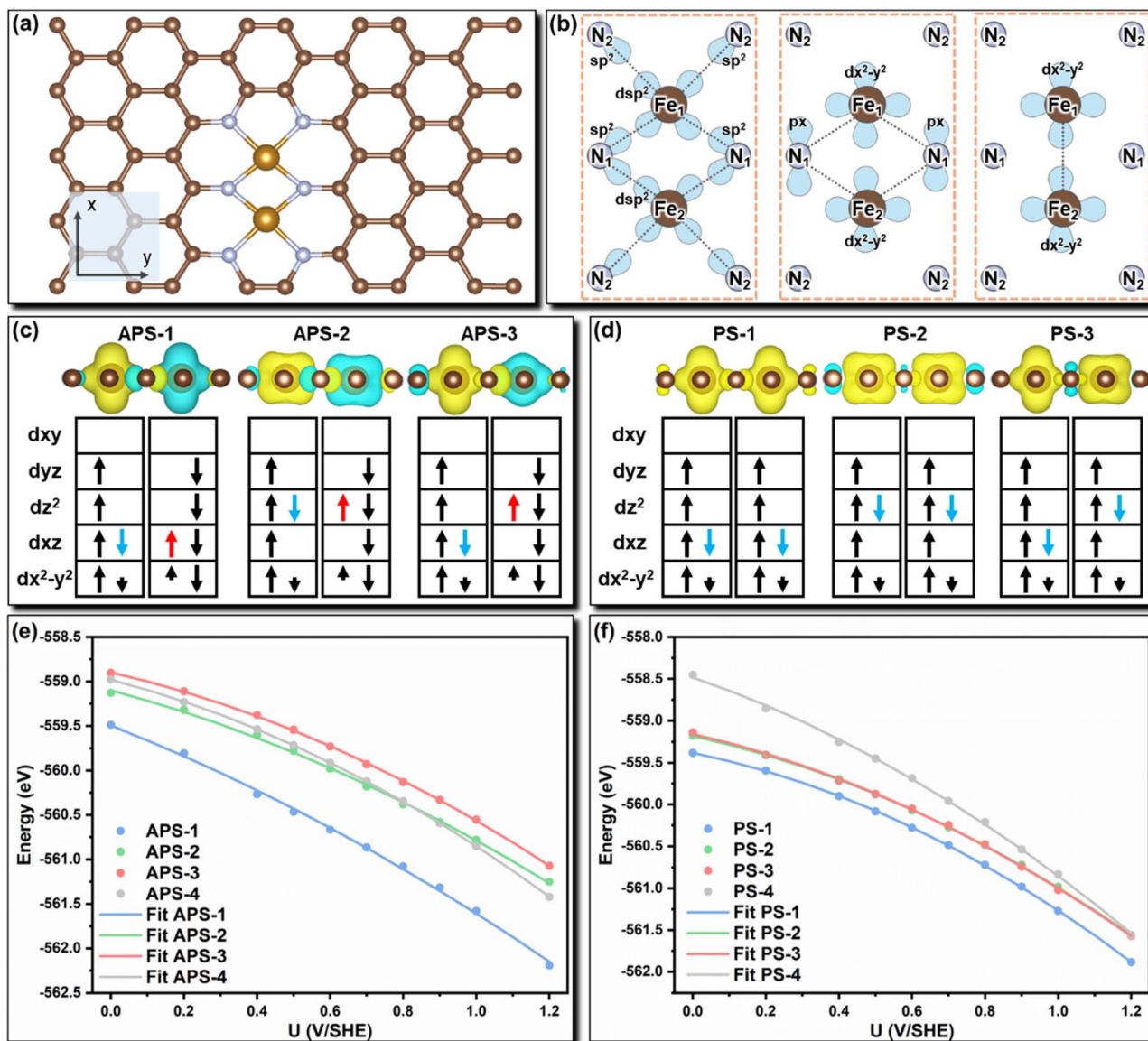
Fig. 2 (a) Model of Fe_2N_6. (b) Schematic diagram of Fe d orbital bonding in Fe_2N_6. (Dashed lines refer to the bonding interaction.) Spin density and d orbital occupation of several stable (c) APS states and (d) PS states of Fe_2N_6. (Smaller arrows refer to partial occupation.) Potential-dependent energies of several (e) APS states and (f) PS states of Fe_2N_6.

from APS-1/PS-1 and APS-2/PS-2, two Fe atoms can hold different occupations on d_{z^2} and d_{xz} orbitals in APS-3 and PS-3. According to PDOS (Fig. S3) and orbital occupancy (Table S4), partial occupation was observed in the $d_{x^2-y^2}$ orbital with the minority spin occupation to be 0.3–0.4 in the APS state and 0.6–0.65 in the PS state, while all the majority spin occupations of the $d_{x^2-y^2}$ orbital are over 0.9. Comparing Fe_2N_6 with the FeN_4 SAC (Table S5) shows that the nonbonding $d_{x^2-y^2}$ orbital holds the spin occupation of 0.016 and 0.878 in HS-FeN_4 and IS-FeN_4, respectively, which suggests more delocalized $d_{x^2-y^2}$ electrons and potential d–d bonding in the DAC, as validated by the COHP analysis in Fig. S6. Finally, the constant-potential energy calculation (Fig. 2e and f) clearly identifies the APS-1 and PS-1 states are the energetically preferable spin states under the ORR operation potential (0–1.2 V vs. SHE), while other spin

states are meta-stable. Thus, these two candidates are treated as two individual DACs with different spin coupling modes and will be used for the subsequent study of ORR activity and mechanism.

Potential-dependent evolution of active centers in APS- and PS-Fe_2N_6

In the Fe_2N_6 DACs, both the Fe sites can catalyze the ORR, which necessitates the exploration of surface configurations and competing reaction pathways. For instance, early studies have shown that O_2 can be absorbed on the bridge site between two TM centers, leading to a new ORR path in Fe_2N_6.[49–51] In addition, as indicated by Li et al., the diatomic site might be dynamically covered by 1–2 OH groups under the operating

potential of ORR, which was known as the self-optimization effect.[52] Moreover, the coexistence of Fe(II) and Fe(III) in partially hydroxylated Fe_2N_6 brings more complicated spin configurations than FeN_4. Thus, it is essential to determine the most stable spin configuration of active moieties. Based on our previous study, we found that the bare FeN_4 unit and the X–FeN_4–Y (X/Y: OOH, O, and OH) complex prefers the IS state, whereas FeN_4–X adopts the HS state.[45] We also tested the multiple spin configurations of Fe_2N_6*OH, as shown in Fig. S7. We observed that the Fe*OH site energetically favors the HS (S = 5/2), while the bare Fe site remained in the IS (S = 1) state. This principle enables quick identification of preferable spin configuration of ORR intermediates in Fe_2N_6. Then, to capture the realistic active center, we established various adsorption models with different OH coverages (Fig. S8) as ORR active sites. The OH adsorption energy of $Fe_2N_6(OH)_n$ was calculated in

reference to previous un-absorbed state $Fe_2N_6(OH)_{n-1}$. We calculated the potential-dependent energy of all the possible structures of Fe_2N_6 with different amounts of OH adsorption in the ORR potential window, as shown in Fig. S9.

According to the number of absorbed OH ligands, we constructed a stepwise potential-dependent adsorption energy curve, as illustrated in Fig. 3a and b. The first OH adsorption shows the transition potential at 0.91 V (APS-Fe_2N_6, Fig. 3a) and 0.62 V (PS-Fe_2N_6, Fig. 3b). The second OH adsorption has three possible locations as shown in Fig. S9b–d and labeled as (i) (HO*OH–*), (ii) (HO*–HO*) and (iii) (HO*–*OH). Within the ORR potential window, configuration (iii) was found to be the most stable in both APS and PS states. The transition potentials are calculated to be 0.87 V (APS) and 0.50 V vs. SHE (PS), respectively. Further OH adsorption beyond two is unfavorable, as shown in the upper panel of Fig. 3a and b. This partially
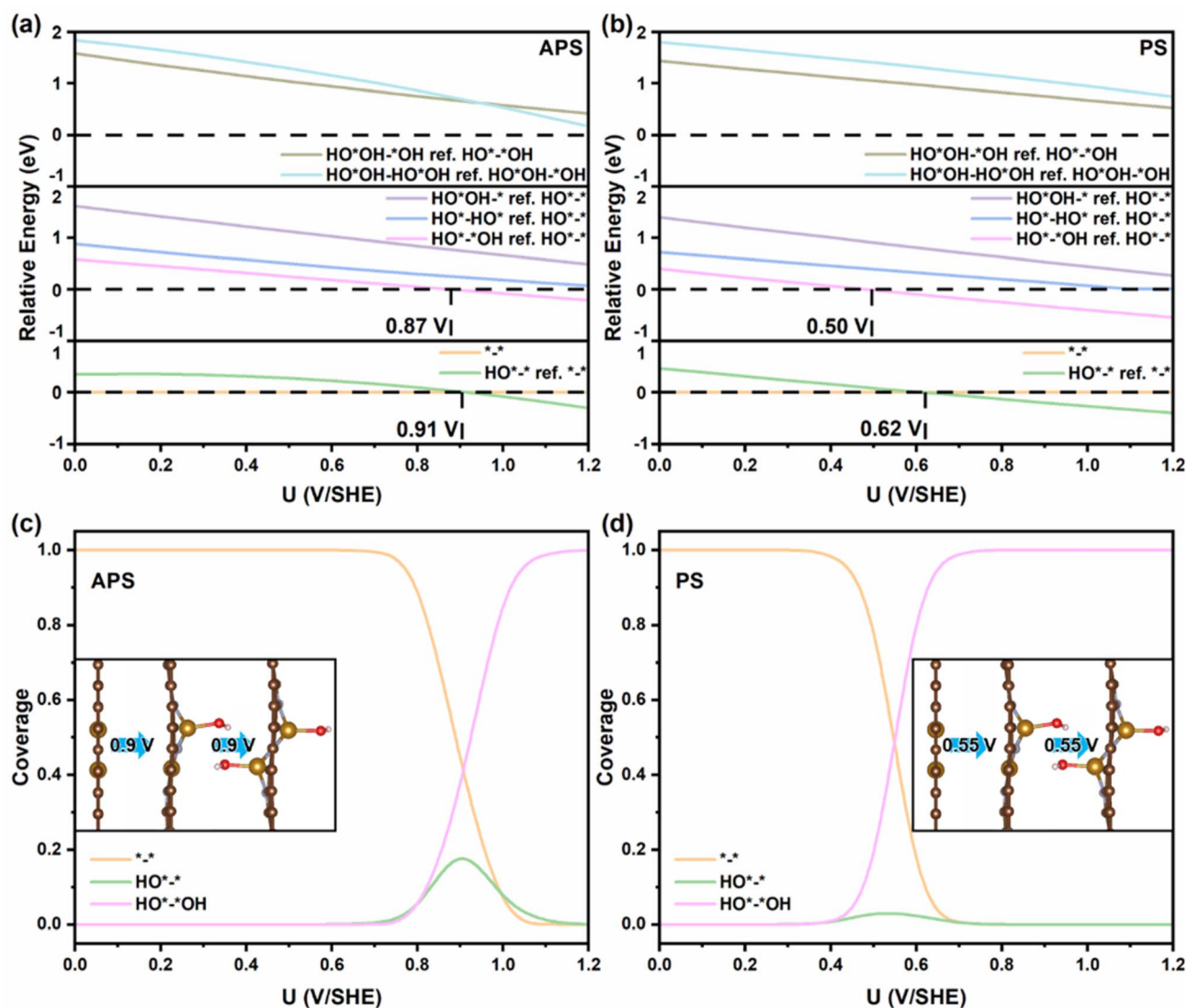

Fig. 3 Phase diagram of OH coverage in (a) antiparallel and (b) parallel Fe_2N_6. (c) Coverage vs. potential of dominant adsorbed OH active sites in antiparallel Fe_2N_6. (d) Coverage vs. potential of dominant adsorbed OH active sites in parallel Fe_2N_6. (Note: "*" refers to the individual active site. "HO*–*" refers to an individual OH absorbed on Fe. "HO*–*OH" refers to the adsorption of two OH ligands absorbed on two Fe separately. "HO*OH–*" refers to the adsorption of two OH ligands absorbed on the same Fe atom, while another Fe has no OH adsorption.)

hydroxylated Fe_2N_6 is consistent with the experimental observation by Li et al.[53] We further calculated the potential-dependent coverage of all OH-absorbed APS- and PS-Fe_2N_6 configurations, as shown in Fig. S10, 3c and d. We found that at transition voltages of 0.9 V and 0.55 V, the APS- and PS-Fe_2N_6 evolved from the bare site *–* to HO*–*OH, while the partition of HO*–* slightly increased but rapidly dropped. In summary, we identified three possible active sites of Fe_2N_6 in the ORR potential range for further mechanistic study.

ORR pathways and activity of APS- and PS-Fe_2N_6

Based on the surface phase diagram in Fig. 3c and d, we now explore the ORR pathways on these active sites. On the bare Fe_2N_6 site, there are two modes of O_2 adsorption: bridge adsorption and end-on adsorption, which lead to different ORR mechanisms, as shown in Fig. S11.[54,55] Free energy of each ORR step on APS- and PS-Fe_2N_6 is shown in Fig. S12–S14 and 4a–d. In the path of end-on O_2 adsorption (Fig. 4a and b), the potential-limiting steps in APS- and PS-Fe_2N_6 are O_2 adsorption and OH desorption with the limiting potentials U_L at 0.78 V and 0.62 V vs. SHE, respectively. In the path of bridge O_2 adsorption, the first step is breaking the O–O bond by protonation to form *OH and *O intermediates on two Fe sites, while the second step has two competing pathways, as shown in Fig. S11b and c. Constant-potential calculation shows that the potential-limiting steps in APS and PS states are O_2 adsorption and *OH desorption with $U_L = 0.51$ V and 0.62 V vs. SHE, respectively (Fig. S14, 4c and d). In addition, it also shows that the O_2 activation (forming *OOH

or HO*–O*) via bridge adsorption is easier than end-on adsorption (Fig. S15), as also reported in previous work.[49] According to the ORR free energy diagram in Fig. S16, we found that the PS-Fe_2N_6 prefers the bridge O_2 adsorption path, while the APS-Fe_2N_6 shows comparable energy in the end-on and bridge O_2 adsorption.

To understand the different capabilities of O_2 activation in APS- and PS-Fe_2N_6, we plotted the potential-dependent COHP analysis on the Fe–O bond in Fig. S17. For bridge O_2 adsorption (Fig. S17a), the Fe–O bond strength (-ICOHP value) decreases with increasing potential in both APS-Fe_2N_6 and PS-Fe_2N_6. In contrast to bridge O_2 adsorption, the Fe–O bond strength (-ICOHP value) increases with increasing potential in the end-on O_2 adsorption (Fig. S17b) case. These results suggest that the bridge and end-on O_2 adsorption exhibit opposite trends in the potential-dependent O_2 activation. With the increase of the electrode potential, end-on O_2 adsorption becomes increasingly favorable, facilitating the O_2 activation, while bridge adsorption mode tends to inhibit O_2 activation with the increase of potential. This discrepancy explains why the end-on O_2 adsorption is more dominant than bridge O_2 adsorption in the ORR catalyzed by Fe_2N_6.

As we discussed in Fig. 2, the partial hydroxylation on Fe results in diverse active sites for ORR catalysis, depending on the OH coverage. Based on the free energy in Fig. S18, 4e and f, the potential-limiting steps of ORR on the HO*–* site were found to be O_2 adsorption and OH desorption in APS- and PS-Fe_2N_6, with limiting potentials of 0.80 V and 0.48 V, respectively.
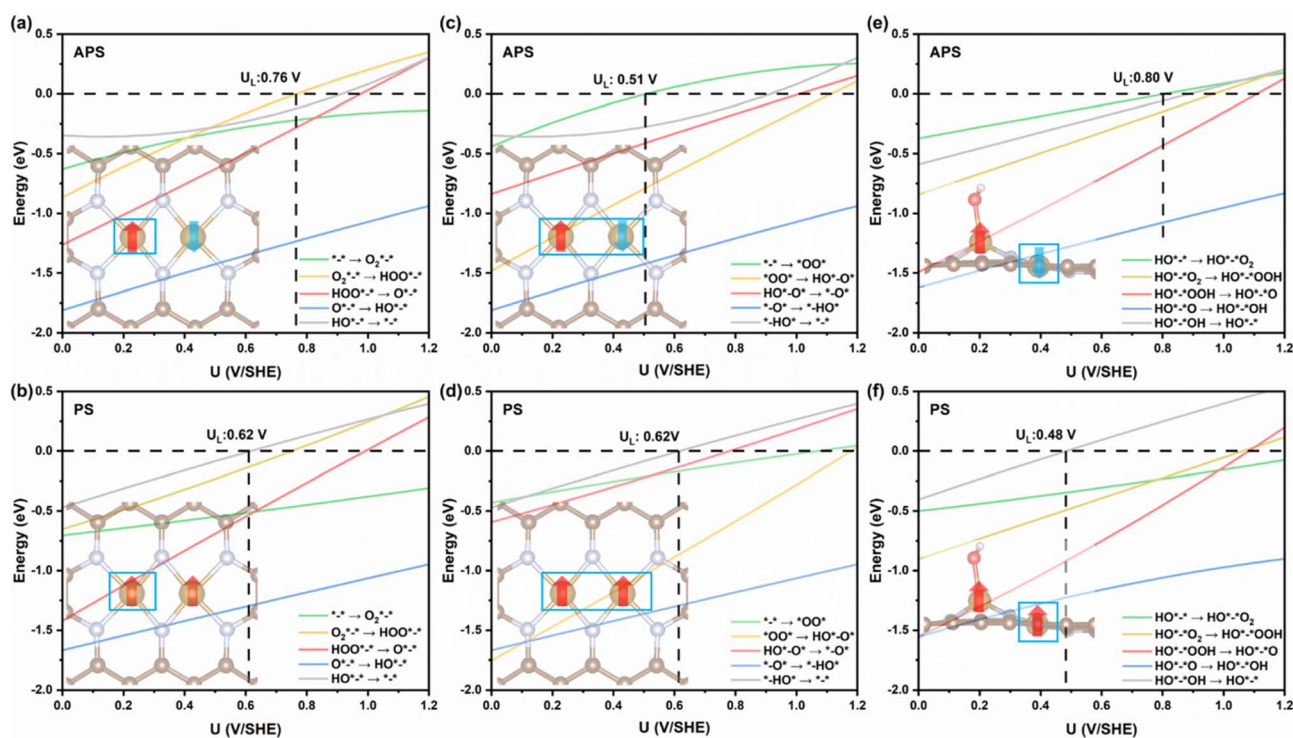

Fig. 4 Potential-dependent reaction free energy of the ORR at a single Fe site in (a) APS- and (b) PS-Fe_2N_6. Potential-dependent reaction free energy of ORR at two Fe sites in (c) APS- and (d) PS-Fe_2N_6. (The reaction path is shown in Fig. S13b.) Potential-dependent reaction free energy of ORR in (e) APS- and (f) PS-HO*Fe_2N_6. (The Fe atoms in the blue frame are the active sites.)

Comparing the U_L values of bare Fe_2N_6 and hydroxylated Fe_2N_6 sites (Fig. 4a–d), it shows that the introduction of OH enhances the ORR activity in APS-Fe_2N_6, while it leads to reduced ORR activity in PS-Fe_2N_6. The active sites with two OH absorbed (HO*–*OH) were also considered, as shown in Fig. S19. In this ORR path, the potential-limiting steps were found to be the OOH formation in both APS- and PS-Fe_2N_6, with limiting potentials at 0.44 V and 0.35 V vs. SHE, respectively. These results indicate that ORR activity is significantly inhibited if two OH groups were pre-absorbed on Fe_2N_6.

Possible competition from two-electron ORR pathways (H_2O_2 formation) was also considered on all active sites. As shown in Fig. S20, on the bare Fe_2N_6 and HO*Fe_2N_6 sites, *OOH energetically tends to form *O instead of H_2O_2. However, on HO*Fe_2N_6*OH, *OOH prefers *O at low potentials but transitions to H_2O_2 formation at 0.94 V (APS) and 0.71 V (PS), suggesting the possibility of a two-electron pathway. The rate-limiting step of the two-electron pathway was found to be O_2 adsorption in the APS state ($U_L = 0.44$ V) and *OOH formation in the PS state ($U_L = 0.35$ V) as shown in Fig. S21. Nevertheless, these U_L values are too low to trigger H_2O_2 formation. Thus, the overall ORR process is still mainly dominated by the four-electron pathway.

Subsequently, based on the ORR pathways and their reaction free energies discussed above, we established a micro-kinetics model and calculated the ORR polarization current of APS- and PS-Fe_2N_6, as shown in Fig. 5. The onset potential is predicted to be 1.05 V and 0.65 V vs. SHE for APS- and PS-Fe_2N_6, respectively, which exhibits superior ORR activity of APS-Fe_2N_6 (Fig. 5a) in comparison to PS-Fe_2N_6 (Fig. 5b) and FeN_4 SAC (Fig. 5c). We note a certain deviation between our predicted onset potential of FeN_4 and experimental results, which can be attributed to the underestimation of adsorption energy caused by the DFT + U method.[56,57] Nevertheless, applying DFT + U is essential for accurately capturing the spin configuration, which is the main purpose of this study. The decomposed polarization current shows that ORR kinetics are mainly dominated by the reaction pathway on the bare site *–* in both APS- and PS-Fe_2N_6, while the other pathways have minor contribution. In summary, here, we validate that the spin coupling mode significantly determines the potential-limiting step (O_2 adsorption in APS vs. OH

desorption in PS) as well as the activity (onset potential: 1.05 V in APS vs. 0.65 V in PS) of the ORR in Fe_2N_6.

Success and limitation of conventional descriptors in the spin-related mechanistic study of the ORR

To understand how spin coupling mode dominates the ORR mechanism, we summarized the potential-limiting steps, U_L values and partial charges of APS-, PS-Fe_2N_6 and FeN_4 SAC, in Table 1. Regardless of the coordination number on Fe, Fe_2N_6 consistently exhibits better ORR activity than FeN_4. The partial charge analysis (Table 1) shows that Fe holds +1.32 $|e|$ and +1.90 $|e|$ charges in FeN_4 and FeN_4*OH, respectively, corresponding to Fe(II) and Fe(III), respectively. Comparing Fe_2N_6 to FeN_4, Fe's partial charge in Fe_2N_6 (including the bare and partially hydroxylated sites) was found to be in the range of 1.32–1.90, indicating their valence located between Fe(II)N_4 and Fe(III) N_4*OH. It can be found that Fe(II)N_4 and Fe(III)N_4*OH show lower potential for *OH desorption and *OOH formation due to their extreme charge distribution, while the charge regulation on Fe_2N_6 optimizes the ORR mechanism and leads to improvement of activity. However, the significantly different ORR mechanisms in APS- and PS-Fe_2N_6 cannot be explained by charge optimization since the change of spin coupling mode has very little impact on the Fe's partial charge (Fig. S22) and charge density difference of adsorbate, as shown in Fig. 6c and e.

Then, we correlate the d orbital occupancy and ORR mechanism in Fe_2N_6 and FeN_4 to interpret the spin coupling effect. As shown in Table 1, we found that the potential-limiting step shifts from *OH desorption to O_2 activation along with the PS–APS transition in Fe_2N_6. The same phenomenon was also observed in FeN_4 when the active center varies from bare FeN_4 to FeN_4*OH, as shown in Fig. S23. These observations suggest that the competition between O_2 activation and OH desorption might be the key factor to determine the ORR activity. According to our previous work, all nonbonding d orbitals (d_{xz}, d_{yz}, d_{z^2}, and $d_{x^2-y^2}$) are potentially capable of bonding with O_2 and OH.[45] This hypothesis has also been validated by Liu et al. and He et al. in various SACs for electrochemical ORR catalysis.[25,58] Therefore, a linear scaling relation between the occupancy of non-bonding d orbitals and U_L was established with R^2 values of 0.69 and
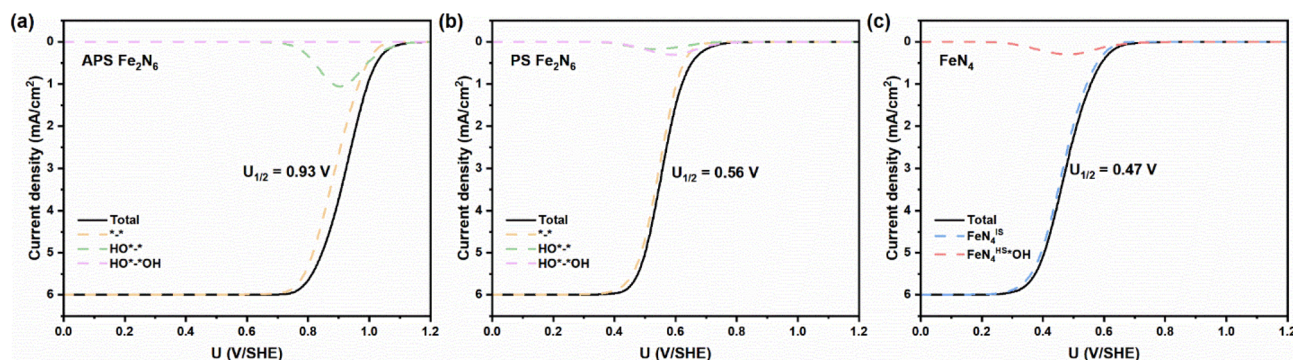

Fig. 5 Simulated ORR polarization current density in (a) APS-Fe_2N_6, (b) PS-Fe_2N_6 and (c) FeN_4. The onset potential is 1.04 V, 0.67 V, and 0.61 V, respectively.

Table 1 Summary of the ORR activity of different pathways and Mulliken charges of active sites in the DAC and SAC. The data of FeN₄ SAC are adopted from our previous work and supplementary calculations[45]

Active site	APS			PS		
	Limiting step	U_L (V vs. SHE)	Mulliken charge	Limiting step	U_L (V vs. SHE)	Mulliken charge
Fe_2N_6/*–* (end-on O_2 adsorption)	OOH formation	0.76	1.36	OH desorption	0.62	1.37
Fe_2N_6/HO*–* (end-on O_2 adsorption)	O_2 adsorption	0.80	1.57	OH desorption	0.48	1.56
Fe_2N_6/HO*–*OH (end-on O_2 adsorption)	OOH formation	0.44	1.78	OOH formation	0.35	1.83
IS/FeN_4*	OH desorption	0.40	1.32			
HS/FeN_4*OH	OOH formation	0.19	1.90			

0.70, as shown in Fig. 6a and b. Without the consideration of APS–PS transition, the overall trend shows that the increase of d orbital occupancy monotonically increases the U_L of O_2 activation (Fig. 6a) and decreases the U_L of *OH desorption (Fig. 6b). This correlation clearly demonstrates that the ORR mechanism in FeN_4, Fe_2N_6, Fe_2N_6*OH, $Fe_2N_6(OH)_2$ and FeN_4OH is determined by the competition between O_2 activation and *OH desorption steps, which are monotonically correlated with the d orbital occupancy of the Fe center. However, it still fails to explain the switch of the ORR mechanism by APS–PS transition in Fe_2N_6 since they show conflicting trends in Fe_2N_6 and Fe_2N_6*OH.

Exchange-splitting-dominated spin-dependent ORR mechanism

Since conventional descriptors (charge and d orbital occupancy) cannot explain the switchable ORR mechanism by APS–PS

transition, one must rethink the role of the spin coupling effect in electrocatalysis. We analyzed the bonding modes and charge transfer characteristics of adsorbed O_2 and OH, as shown in Fig. 6c and e. We found that both the charge transfer and Fe–O bonding configurations are essentially identical in the APS and PS states, with electrons occupying the Fe–O antibonding orbitals. The key distinction lies in the spin coupling between neighboring Fe sites, which alters the coupling behavior of the $d_{x^2-y^2}$ orbitals: APS coupling reduces the spin, while PS enhances the spin. According to our hypothesis, the spin-polarized bond of catalyst-adsorbate can be effectively tuned by the spin coupling from the neighboring magnetic site or external field, leading to the change of bonding strength (Fig. 1). To validate this point, we calculated the energy of bonding and antibonding orbitals of the Fe–O bond in APS- and PS-Fe_2N_6 with OH and O_2 adsorption via COHP analysis, as shown in Fig. 6d and f. It can be clearly found that APS–PS transition
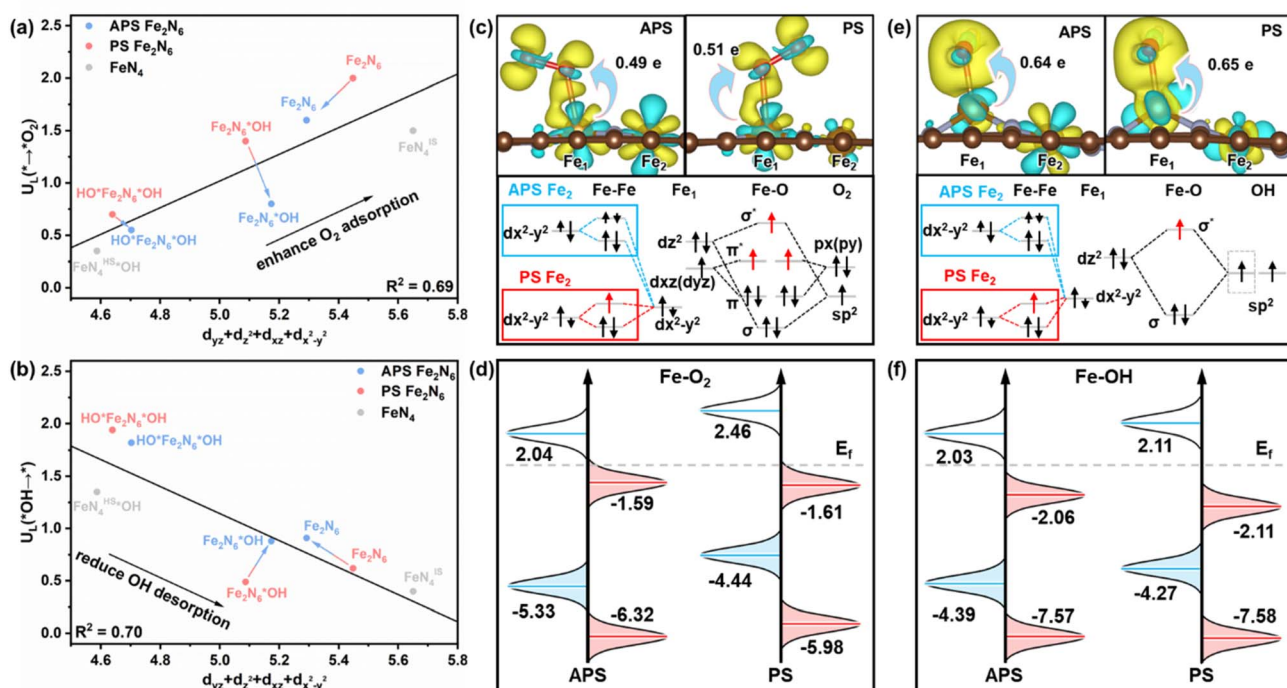

Fig. 6 Correlation between the sum of the four d orbitals' occupancy (d_{yz}, d_{z^2}, d_{xz} and $d_{x^2-y^2}$) and the (a) limiting potential of O_2 adsorption and (b) limiting potential of OH desorption. (c) Charge transfer diagram of Fe_2N_6*O_2 and Fe–O bond orbitals. (d) Bonding and antibonding centers of Fe–O in Fe_2N_6*O_2. (e) Charge transfer diagram of Fe_2N_6*OH and Fe–O bond orbitals. (f) Bonding and antibonding centers of Fe–O in Fe_2N_6*OH.

pushes up the energy of unfilled spin-down σ^*(Fe–O) (from 2.04 eV to 2.46 eV) and pushes down the spin-up σ^*(Fe–O) (−1.59 eV to −1.61 eV) in $Fe_2N_6^*O_2$ (Fig. 6d). Similar trends can also be found in $Fe_2N_6^*OH$, as shown in Fig. 6f. This can be explained by the influence of spin exchange splitting, as widely reported in spintronic materials.[59,60]

With the upshift of energy of the unfilled spin-down σ^*(Fe–O) orbital ($E_{\sigma^*}^{down}$), the electron filling should become more difficult, stabilizing the adsorbate on the catalyst and strengthening the Fe–O bond. To validate this explanation, we summarized the energy of the spin-down σ^*(Fe–O) orbital and the limiting potential (O_2 activation and OH desorption steps) in Fig. 7. As shown in Fig. 7a, the energy of spin-down σ^*(Fe–O) was pushed up when the spin coupling mode switches from APS to PS, which is consistent with our proposed mechanism in Fig. 1. At the same time, as shown in Fig. 7b, the O_2 activation potential increases, while the OH desorption potential decreases after APS–PS transition, indicating the enhanced binding of O_2 and OH on the Fe site. These results provide convincing evidence to show that the exchange splitting determines the strength of the Fe–O bond and ORR mechanism in Fe_2N_6 DAC. This also explains the change of limiting steps from O_2 activation to OH desorption through APS–PS transition in Fig. 6 and Table 1. Similarly, for other ORR intermediates, such as *O and *OOH, the Fe–O bond also has similar electron occupation to Fe*OH where the spin electron only fills the spin-up component of the antibonding orbital, as shown in Fig. S24a. The energy of the spin-down Fe–O antibonding orbital is shifted up by APS–PS transition, leading to enhanced adsorption of *O and *OOH (Fig. S24b and c).

To validate the extendibility of this mechanism, we further calculate the ORR mechanism of isomerized Fe_2N_6 (consisting of two FeN_3 moieties, denoted as $(FeN_3)_2$) and bi-metallic $MFeN_6$ DAC. As shown in Fig. S25 and S26, the ORR occurs on the bridge site of $(FeN_3)_2$ and is dominated by the path of $(FeN_3)_2^*OH$ (Fig. S26f) instead of bare $(FeN_3)_2$ (Fig. S26c). Due to the Fe–O–Fe bond formation (breaking) at the OH desorption (O_2 activation) step accompanied by Fe flip (Fig. S26f), the ORR mechanism is not changed by APS–PS transition although the

limiting potential decreases from 0.55 V to 0.45 V. The complex ORR mechanism that associates synergic steps on dual sites make the contribution of spin coupling undistinguishable. To separately validate the crucial role of the spin coupling effect, we studied the ORR mechanism on the bi-metallic $MFeN_6$ DACs, which possess the same geometry and ORR path. As shown in Fig. 8, by flipping the spin of element M (M = Mn, Co, Ni), we calculated the potential of O_2 activation and OH desorption on the Fe site. It shows that switching APS to PS leads to the increase of U_L (O_2) and decrease of U_L (OH desorption), which are in good agreement with our proposed mechanism. These results suggest that flipping the spin of adjacent atoms is an effective and controllable strategy to alter the catalytic activity of DACs or similar magnetic catalysts.

Implication of our work for experiments and theories

Our work reveals how spin coupling modulates the ORR mechanism and activity of DAC, which differs from the conventional strategy of directly tuning the spin state of active sites. From an experimental perspective, although controlling the spin alignment of DACs is still challenging at the current stage, we still found some experimental clues to support the feasibility of this strategy. Gao et al. in 2017 reported the interatomic spin coupling of Mn clusters supported on graphene with APS-type spin alignment and a controllable spin state by the external magnetic field, which is comparable to the Fe_2N_6 DAC.[61] In addition, the PS/APS configuration is similar to ferro-antiferromagnetic coupling, which can be switching by adjusting the spin exchange energy. Xu et al. applied continuous tensile strain to two-dimensional materials and achieved a reversible strain-induced antiferromagnetic–ferromagnetic phase transition, showing the potential feasibility of strain engineering in tuning the spin configuration of electrocatalysts.[62] A simple validation was also done in our study (Fig. S27), which shows that APS–PS transition of Fe_2N_6 can be achieved at a biaxial tensile strain over 4%. However, this spin state manipulation by strain engineering in Fe_2N_6 for enhanced ORR activity needs further experimental effort due to the challenge of searching for an appropriate substrate.
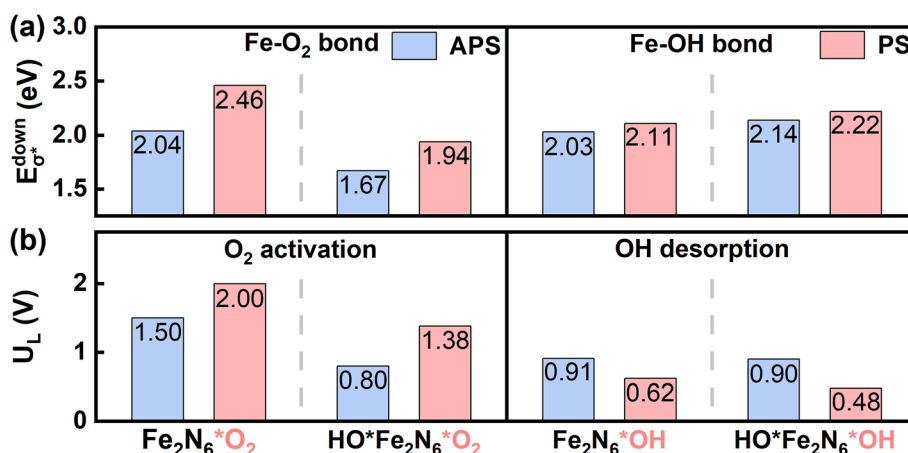

Fig. 7 (a) Energy shift of the spin-down σ^*(Fe–O) orbital and (b) change of the limiting potential in O_2 activation and OH desorption steps.
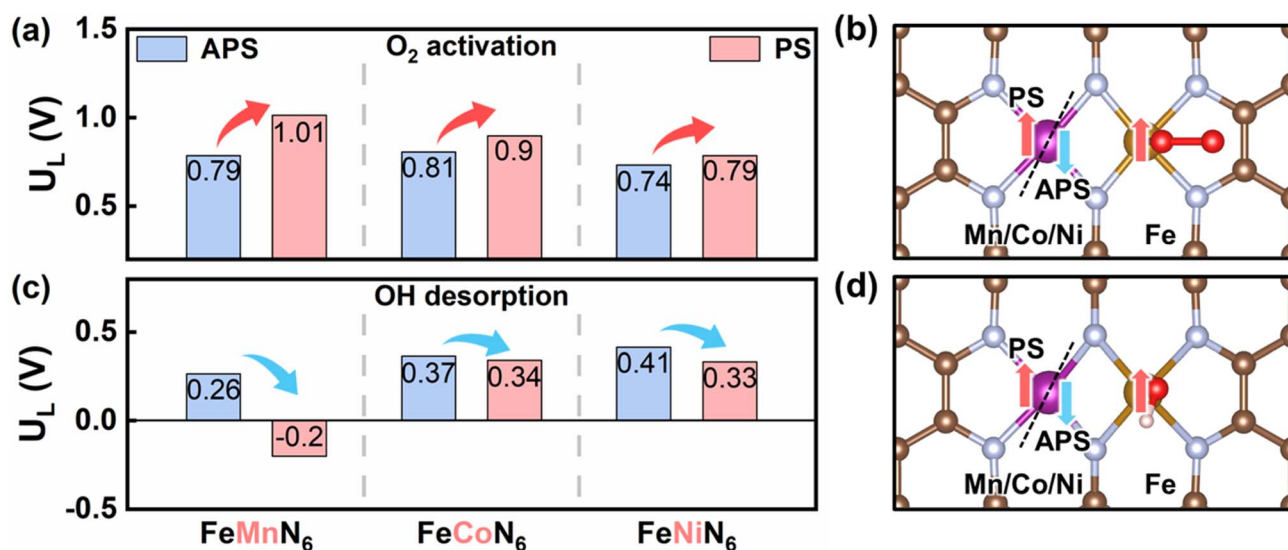
Fig. 8 (a) U_L of O_2 activation steps and (b) structure of bi-metallic $FeMN_6*O_2$. (c) U_L of OH desorption steps and (d) structure of bi-metallic $MFeN_6*OH$.

From the theoretical perspective, our study clearly shows the significance of tuning the intermetallic spin coupling mode in DACs. In addition to the metal–metal spin coupling, a recent study has indicated that the spin coupling between Fe and triplet O_2 also significantly influences the ORR mechanism on Fe–N–C SACs.[63] This finding enriches the physical picture and definition of the spin coupling effect in electrocatalysis, underlining the significance of spin configuration in the first-principles electrochemical simulation. Deciphering the spin coupling effects, including both site–site and site–adsorbate spin coupling, is a potentially practical way to elucidate the mechanism of magnetic-field-assisted electrocatalysis. We believe our study can be further applied to understand how an external field influences the magnetic domain and enhances the activity, as experimentally observed by Wu *et al.*[64] Moreover, considering the tremendous possible configurations of M–N–C DACs,[65] we believe that most of these DACs with a suitable M–M distance that enables spin exchange splitting should have the tunable activity/mechanism *via* tuning the spin alignment. We hope our study can bring attention to the spin coupling effect and its potential application in electrocatalysis.

Summary and conclusion

In this study, we proposed a general mechanism to explore how spin coupling alters the catalytic mechanism *via* exchange splitting of the catalyst–adsorbate bond. Taking the ORR in the Fe_2N_6 DAC as an example, we validated that the APS–PS transition significantly determines the ORR mechanism and activity, while conventional electronic descriptors cannot explain this phenomenon. This spin-dominated mechanism transition is determined by the exchange splitting of the $\sigma*$(Fe–O) orbital, which is significantly controlled by spin alignment. The enhanced exchange splitting in the PS state leads to stronger Fe–O bonding and worse ORR activity due to the over-

binding of OH, while weakened exchange splitting in the APS state alters the Fe–O bond to a suitable degree, leading to promising ORR activity. We also validate this mechanism in other bi-metallic DACs, including $MnFeN_6$, $CoFeN_6$ and $NiFeN_6$. These DACs consistently show enhanced OH and O_2 adsorption after APS–PS transition, thereby validating the extendibility of our mechanism. Thus, our work provides a general theory to guide the theoretical design of spin electrocatalysts by tuning the spin exchange splitting and spin alignment.

Author contributions

C. Z. designed the project. M. Y. performed the simulation, data analysis, and manuscript writing. M. Y., E. K. and C. Z. participated in the discussion and manuscript revision.

Conflicts of interest

There are no conflicts to declare.

Data availability

Acknowledgements

References

1 Y. Wang, H. Su, Y. He, L. Li, S. Zhu, H. Shen, P. Xie, X. Fu, G. Zhou and C. Feng, Advanced Electrocatalysts with Single-Metal-Atom Active Sites, *Chem. Rev.*, 2020, **120**(21), 12217–12314.

2 J. Liu, Catalysis by Supported Single Metal Atoms, *ACS Catal.*, 2017, **7**(1), 34–59.

3 X. Yang, A. Wang, B. Qiao, J. Li, J. Liu and T. Zhang, Single-Atom Catalysts: A New Frontier in Heterogeneous Catalysis, *Acc. Chem. Res.*, 2013, **46**(8), 1740–1748.

4 S. Wang, M. Luo and S. Guo, Two Atoms Are Better Than One, *Nat. Synth.*, 2022, **1**(9), 676–677.

5 Y. Xie, X. Chen, K. Sun, J. Zhang, W. H. Lai, H. Liu and G. Wang, Direct Oxygen-Oxygen Cleavage through Optimizing Interatomic Distances in Dual Single-Atom Electrocatalysts for Efficient Oxygen Reduction Reaction, *Angew. Chem., Int. Ed.*, 2023, **135**(17), e202301833.

6 Y. Deng, J. Luo, B. Chi, H. Tang, J. Li, X. Qiao, Y. Shen, Y. Yang, C. Jia and P. Rao, Advanced Atomically Dispersed Metal-Nitrogen-Carbon Catalysts toward Cathodic Oxygen Reduction in Pem Fuel Cells, *Adv. Energy Mater.*, 2021, **11**(37), 2101222.

7 R. Li and D. Wang, Superiority of Dual-Atom Catalysts in Electrocatalysis: One Step Further Than Single-Atom Catalysts, *Adv. Energy Mater.*, 2022, **12**(9), 2103564.

8 W. Zhang, Y. Chao, W. Zhang, J. Zhou, F. Lv, K. Wang, F. Lin, H. Luo, J. Li and M. Tong, Emerging Dual-Atomic-Site Catalysts for Efficient Energy Catalysis, *Adv. Mater.*, 2021, **33**(36), 2102576.

9 Y. Li, Y. Li, H. Sun, L. Gao, X. Jin, Y. Li, Z. Lv, L. Xu, W. Liu and X. Sun, Current Status and Perspectives of Dual-Atom Catalysts Towards Sustainable Energy Utilization, *Nano-Micro Lett.*, 2024, **16**(1), 139.

10 Z. Wang, M. Cheng, Y. Liu, Z. Wu, H. Gu, Y. Huang, L. Zhang and X. Liu, Dual-Atomic-Site Catalysts for Molecular Oxygen Activation in Heterogeneous Thermo-/Electro-Catalysis, *Angew. Chem., Int. Ed.*, 2023, **135**(22), e202301483.

11 X. Han, J. Chen, P. He and J. Lu, Harnessing Spin Effects for Heterogeneous Single-Atom Spin Catalysis, *Natl. Sci. Rev.*, 2024, **11**(9), nwae217.

12 A. Yu, Y. Zhang, S. Zhu, T. Wu and Z. J. Xu, Spin-Related and Non-Spin-Related Effects of Magnetic Fields on Water Oxidation, *Nat. Energy*, 2025, 1–13.

13 C. Chen, Y. Wu, X. Li, Y. Ye, Z. Li, Y. Zhou, J. Chen, M. Yang, F. Xie and Y. Jin, Modulating Fe Spin State in Fenc Catalysts by Adjacent Fe Atomic Clusters to Facilitate Oxygen Reduction Reaction in Proton Exchange Membrane Fuel Cell, *Appl. Catal., B*, 2024, **342**, 123407.

14 H. Zhang, H. C. Chen, S. Feizpoor, L. Li, X. Zhang, X. Xu, Z. Zhuang, Z. Li, W. Hu, R. Snyders, W. Dingsheng and W. Chundong, Tailoring Oxygen Reduction Reaction Kinetics of Fe-N-C Catalyst Via Spin Manipulation for Efficient Zinc-Air Batteries, *Adv. Mater.*, 2024, **36**(25), 2400523.

15 J. Zhang, F. Li, W. Liu, Q. Wang, X. Li, S. Hung, H. Yang and B. Liu, Modulating Spin of Atomic Manganese Center for High-Performance Oxygen Reduction Reaction, *Angew. Chem., Int. Ed.*, 2024, **63**(51), e202412245.

16 Z. Zhuang, Y. Li, Y. Li, J. Huang, B. Wei, R. Sun, Y. Ren, J. Ding, J. Zhu and Z. Lang, Atomically Dispersed Nonmagnetic Electron Traps Improve Oxygen Reduction Activity of Perovskite Oxides, *Energy Environ. Sci.*, 2021, **14**(2), 1016–1028.

17 D. Xue, Y. Yuan, Y. Yu, S. Xu, Y. Wei, J. Zhang, H. Guo, M. Shao and J. Zhang, Spin Occupancy Regulation of the Pt d-orbital for a Robust Low-Pt Catalyst Towards Oxygen Reduction, *Nat. Commun.*, 2024, **15**(1), 5990.

18 W. Cheng, P. Yuan, Z. Lv, Y. Guo, Y. Qiao, X. Xue, X. Liu, W. Bai, K. Wang, Q. Xu and J. Zhang, Boosting Defective Carbon by Anchoring Well-Defined Atomically Dispersed Metal-N$_4$ Sites for ORR, OER, and Zn-Air Batteries, *Appl. Catal., B*, 2020, **260**, 118198.

19 Y. Cui, C. Ren, Q. Li, C. Ling and J. Wang, Hybridization State Transition under Working Conditions: Activity Origin of Single-Atom Catalysts, *J. Am. Chem. Soc.*, 2024, **146**(22), 15640–15647.

20 G. Yang, J. Zhu, P. Yuan, Y. Hu, G. Qu, B. Lu, X. Xue, H. Yin, W. Cheng, J. Cheng, X. Wenjing, L. Jin, H. Jingsong, M. Shichun and J. Zhang, Regulating Fe-Spin State by Atomically Dispersed Mn-N in Fe-NC Catalysts with High Oxygen Reduction Activity, *Nat. Commun.*, 2021, **12**(1), 1734.

21 Z. Chen, H. Niu, J. Ding, H. Liu, P. H. Chen, Y. H. Lu, Y. R. Lu, W. Zuo, L. Han and Y. Guo, Unraveling the Origin of Sulfur-Doped Fe-N-C Single-Atom Catalyst for Enhanced Oxygen Reduction Activity: Effect of Iron Spin-State Tuning, *Angew. Chem., Int. Ed.*, 2021, **133**(48), 25608–25614.

22 F. Sun, F. Li and Q. Tang, Spin State as a Participator for Demetalation Durability and Activity of Fe-N-C Electrocatalysts, *J. Phys. Chem. C*, 2022, **126**(31), 13168–13181.

23 W. Zhong, Y. Qiu, H. Shen, X. Wang, J. Yuan, C. Jia, S. Bi and J. Jiang, Electronic Spin Moment as a Catalytic Descriptor for Fe Single-Atom Catalysts Supported on C$_2$N, *J. Am. Chem. Soc.*, 2021, **143**(11), 4405–4413.

24 P. Liu, H. Liu, Y. Qiu, J. Jiang and W. Zhong, Electron Transfer Induced by the Change of Spin States as a Catalytic Descriptor on C$_2$N-Tm Single-Atom Catalysts, *J. Phys. Chem. Lett.*, 2024, **15**(35), 9003–9009.

25 K. Liu, J. Fu, Y. Lin, T. Luo, G. Ni, H. Li, Z. Lin and M. Liu, Insights into the Activity of Single-Atom Fe-NC Catalysts for Oxygen Reduction Reaction, *Nat. Commun.*, 2022, **13**(1), 2075.

26 F. Wang, L. Hu and Y. Jing, Correlation between the Spin Effect and Catalytic Activity of Two-Dimensional Metal Organic Frameworks for the Oxygen Evolution Reaction, *J. Mater. Chem. A*, 2024, **12**(42), 28764–28770.

27 T. Sun, Z. Tang, W. Zang, Z. Li, J. Li, Z. Li, L. Cao, J. S. Dominic Rodriguez, C. O. M. Mariano and H. Xu, Ferromagnetic Single-Atom Spin Catalyst for Boosting Water Splitting, *Nat. Nanotechnol.*, 2023, **18**(7), 763–771.

28 L. Yu, F. Li, J. Zhao and Z. Chen, Revisiting Catalytic Performance of Supported Metal Dimers for Oxygen Reduction Reaction *Via* Magnetic Coupling from First Principles, *Adv. Powder Mater.*, 2022, **1**(3), 100031.

29 Z. Wang, Y. Chen, S. Fang, X. Zhang, W. Zhang, F. Sun, W. Chen and G. Zhuang, Magnetic Transition of 1D Ferromagnetic Catalysts During the NO Electroreduction, *J. Catal.*, 2024, **434**, 115524.

30 S. Fang, Y. Chen, W. Chen and G. Zhuang, Magnetic Order Transition of a Two-Dimensional Square-Lattice Electrocatalyst Assembled by Fe-N$_4$ Units: Crucial Role on Oxygen Reduction, *J. Phys. Chem. Lett.*, 2024, **15**(22), 5887–5895.

31 Z. Jin, P. Li, Y. Meng, Z. Fang, D. Xiao and G. Yu, Understanding the Inter-Site Distance Effect in Single-Atom Catalysts for Oxygen Electroreduction, *Nat. Catal.*, 2021, **4**(7), 615–622.

32 K. Zhang, A. Cao, L. H. Wandall, J. Vernieres, J. Kibsgaard, J. K. Nørskov and I. Chorkendorff, Spin-Mediated Promotion of Co Catalysts for Ammonia Synthesis, *Science*, 2024, **383**(6689), 1357–1363.

33 P. E. Blöchl, Projector Augmented-Wave Method, *Phys. Rev. B:Condens. Matter Mater. Phys.*, 1994, **50**(24), 17953.

34 G. Kresse and J. Furthmüller, Efficiency of *ab initio* Total Energy Calculations for Metals and Semiconductors Using a Plane-Wave Basis Set, *Comput. Mater. Sci.*, 1996, **6**(1), 15–50.

35 G. Kresse and D. Joubert, From Ultrasoft Pseudopotentials to the Projector Augmented-Wave Method, *Phys. Rev. B:Condens. Matter Mater. Phys.*, 1999, **59**(3), 1758.

36 J. P. Perdew, K. Burke and M. Ernzerhof, Generalized Gradient Approximation Made Simple, *Phys. Rev. Lett.*, 1996, **77**(18), 3865.

37 S. Grimme, Semiempirical GGA-Type Density Functional Constructed with a Long-Range Dispersion Correction, *J. Comput. Chem.*, 2006, **27**(15), 1787–1799.

38 M. Yu, A. Li, E. Kan and C. Zhan, Substantial Impact of Spin State Evolution in OER/ORR Catalyzed by Fe-N-C, *ACS Catal.*, 2024, **14**(9), 6816–6826.

39 V. Wang, N. Xu, J. Liu, G. Tang and W. Geng, Vaspkit: A User-Friendly Interface Facilitating High-Throughput Computing and Analysis Using Vasp Code, *Comput. Phys. Commun.*, 2021, **267**, 108033.

40 V. L. Deringer, A. L. Tchougréeff and R. Dronskowski, Crystal Orbital Hamilton Population (COHP) Analysis as Projected from Plane-Wave Basis Sets, *J. Phys. Chem. A*, 2011, **115**(21), 5461–5466.

41 S. Maintz, V. L. Deringer, A. L. Tchougréeff and R. Dronskowski, LOBSTER: A Tool to Extract Chemical Bonding from Plane-Wave Based DFT, *J. Comput. Chem.*, 2016, **37**(11), 1030–1035.

42 Z. Duan and P. Xiao, Simulation of Potential-Dependent Activation Energies in Electrocatalysis: Mechanism of O-O Bond Formation on RuO$_2$, *J. Phys. Chem. C*, 2021, **125**(28), 15243–15250.

43 K. Letchworth-Weaver and T. A. Arias, Joint Density Functional Theory of the Electrode-Electrolyte Interface: Application to Fixed Electrode Potentials, Interfacial Capacitances, and Potentials of Zero Charge, *Phys. Rev. B:Condens. Matter Mater. Phys.*, 2012, **86**(7), 075140.

44 Y. Huang, R. J. Nielsen and W. A. Goddard III, Reaction Mechanism for the Hydrogen Evolution Reaction on the Basal Plane Sulfur Vacancy Site of MoS$_2$ Using Grand Canonical Potential Kinetics, *J. Am. Chem. Soc.*, 2018, **140**(48), 16773–16782.

45 M. Yu, J. Wu, Y. Chen, Y. Du, A. Li, E. Kan and C. Zhan, Strain-Controlled Spin Regulation in Fe-N-C Catalysts for Enhanced Oxygen Reduction Reaction Activity, *J. Mater. Chem. A*, 2024, **12**(36), 24530–24541.

46 B. Dorado, B. Amadon, M. Freyss and M. Bertolus, DFT+ U Calculations of the Ground State and Metastable States of Uranium Dioxide, *Phys. Rev. B:Condens. Matter Mater. Phys.*, 2009, **79**(23), 235125.

47 J. P. Allen and G. W. Watson, Occupation Matrix Control of d- and f-electron Localisations Using DFT+U, *Phys. Chem. Chem. Phys.*, 2014, **16**(39), 21016–21031.

48 T. Zheng, J. Wang, Z. Xia, G. Wang and Z. Duan, Spin-Dependent Active Centers in Fe-N-C Oxygen Reduction Catalysts Revealed by Constant-Potential Density Functional Theory, *J. Mater. Chem. A*, 2023, **11**(36), 19360–19373.

49 Z. Huang, M. Li, X. Yang, T. Zhang, X. Wang, W. Song, J. Zhang, H. Wang, Y. Chen and J. Ding, Diatomic Iron with a Pseudo-Phthalocyanine Coordination Environment for Highly Efficient Oxygen Reduction over 150,000 Cycles, *J. Am. Chem. Soc.*, 2024, **146**(36), 24842–24854.

50 J. Liu, H. Xu, J. Zhu and D. Cheng, Understanding the Pathway Switch of the Oxygen Reduction Reaction from Single-to Double-/Triple-Atom Catalysts: A Dual Channel for Electron Acceptance-Backdonation, *JACS Au*, 2023, **3**(11), 3031–3044.

51 M. Liu, X. Wang, S. Cao, X. Lu, W. Li, N. Li and X. H. Bu, Ferredoxin-Inspired Design of S-Synergized Fe-Fe Dual-Metal Center Catalysts for Enhanced Electrocatalytic Oxygen Reduction Reaction, *Adv. Mater.*, 2024, **36**(19), 2309231.

52 D. Li, P. Sun, H. Xu, J. Yun and D. A. Cao, Revised High-Throughput Screening Model on Oxygen Reduction Reaction over Dual Atom Catalysts Based on the Axial Pre-Adsorption and O$_2$ Adsorption, *Adv. Energy Mater.*, 2024, 2403524.

53 L. Yan, Y. Mao, Y. Li, Q. Sha, K. Sun, P. Li, G. I. Waterhouse, Z. Wang, S. Tian and X. Sun, Sublimation Transformation Synthesis of Dual-Atom Fe Catalysts for Efficient Oxygen Reduction Reaction, *Angew. Chem., Int. Ed.*, 2024, e202413179.

54 W. Zhang, S. Yi, Y. Yu, H. Liu, A. Kucernak, J. Wu and L. Song, Fe-Based Dual-Atom Catalysts for Oxygen Reduction Reaction, *J. Mater. Chem. A*, 2023, **12**, 87–112.

55 M. Xiao, Y. Chen, J. Zhu, H. Zhang, X. Zhao, L. Gao, X. Wang, J. Zhao, J. Ge and Z. Jiang, Climbing the Apex of the ORR Volcano Plot *Via* Binuclear Site Construction: Electronic and Geometric Engineering, *J. Am. Chem. Soc.*, 2019, **141**(44), 17763–17770.

56 Y. Wang, Y. Tang and K. Zhou, Self-Adjusting Activity Induced by Intrinsic Reaction Intermediate in Fe-N-C Single-Atom Catalysts, *J. Am. Chem. Soc.*, 2019, **141**(36), 14115–14119.

57 Y. Jin, M. Yu, E. Kan and C. Zhan, Synergistic Spin-Ligand Effects on the Oxygen Reduction Activity of Feppc Electrocatalyst, *J. Mater. Chem. A*, 2025, **13**(30), 24831–24839.

58 C. He, C. Lee, L. Meng, H. T. Chen and Z. Li, Selective Orbital Coupling: An Adsorption Mechanism in Single-Atom Catalysis, *J. Am. Chem. Soc.*, 2024, **146**(18), 12395–12400.

59 A. León, E. A. Velasquez, F. J. Torres, J. MejíaLópez and P. Vargas, Hydrogen Induced AFM to FM Magnetic Transition in ε-FeH$_x$, *J. Magn. Magn. Mater.*, 2020, **498**, 166147.

60 M. Z. Kasiab, K. Tadele, M. A. Afrassa and O. Akin-Ojo, First-Principles Study of Superconducting in LiFeAs: FM, AFM, and NM States *Via* DFT and DFT+U Techniques, *AIP Adv.*, 2025, **15**(5), 055110.

61 J. Ren, H. Guo, J. Pan, Y. Zhang, Y. Yang, X. Wu, S. Du, M. Ouyang and H. Gao, Interatomic Spin Coupling in Manganese Clusters Registered on Graphene, *Phys. Rev. Lett.*, 2017, **119**(17), 176806.

62 Z. Fang, R. Chen, J. Zheng, A. I. Khan, K. M. Neilson, S. J. Geiger, D. M. Callahan, M. G. Moebius, A. Saxena and M. E. Chen, Ultra-Low-Energy Programmable Non-Volatile Silicon Photonics Based on Phase-Change Materials with Graphene Heaters, *Nat. Nanotechnol.*, 2022, **17**(8), 842–848.

63 J. Xie and Z. Duan, Spin-Orientation-Dependent O_2 Adsorption Mechanism in Fe Single-Atom Catalysts, *J. Phys. Chem. C.*, 2024, **128**(49), 20819–20826.

64 T. Wu, J. Ge, Q. Wu, X. Ren, F. Meng, J. Wang, S. Xi, X. Wang, K. Elouarzaki, A. Fisher and Z. J. Xu, Tailoring Atomic Chemistry to Refine Reaction Pathway for the Most Enhancement by Magnetization in Water Oxidation, *Proc. Natl. Acad. Sci. U. S. A.*, 2024, **121**(19), e2318652121.

65 C. Brea and G. Hu, Mechanistic Insight into Dual-Metal-Site Catalysts for the Oxygen Reduction Reaction, *ACS Catal.*, 2023, **13**(7), 4992–4999.